Universal motion of mirror-symmetric microparticles in confined Stokes flow

Rumen N. Georgiev[a] (ID), Sara O. Toscano[a], William E. Uspal[b], Bram Bet[c], Sela Samin[c], René van Roij[c] (ID), and Huseyin Burak Eral[a,d,1] (ID)

[a]Process and Energy Department, Delft University of Technology, 2628CB Delft, The Netherlands; [b]Department of Mechanical Engineering, University of Hawaii at Manoa, Honolulu, HI 96822; [c]Institute for Theoretical Physics, Center for Extreme Matter and Emergent Phenomena, Utrecht University, 3584 CC Utrecht, The Netherlands; and [d]Van't Hoff Laboratory for Physical and Colloid Chemistry, Debye Institute, Utrecht University, 3584 CH Utrecht, The Netherlands

Comprehensive understanding of particle motion in microfluidic devices is essential to unlock additional technologies for shape-based separation and sorting of microparticles like microplastics, cells, and crystal polymorphs. Such particles interact hydrodynamically with confining surfaces, thus altering their trajectories. These hydrodynamic interactions are shape dependent and can be tuned to guide a particle along a specific path. We produce strongly confined particles with various shapes in a shallow microfluidic channel via stop flow lithography. Regardless of their exact shape, particles with a single mirror plane have identical modes of motion: in-plane rotation and cross-stream translation along a bell-shaped path. Each mode has a characteristic time, determined by particle geometry. Furthermore, each particle trajectory can be scaled by its respective characteristic times onto two master curves. We propose minimalistic relations linking these timescales to particle shape. Together these master curves yield a trajectory universal to particles with a single mirror plane.

microfluidics | Hele–Shaw flow | particle-laden flow

Separation on the microscale is a persistent industrial challenge: Pharmaceutical crystal polymorphs (1, 2), specific strains of yeast cells in the food industry (3), mammalian cells (4), and microplastic pollutants (5, 6) all come in different shapes, yet comparable sizes. Advances in microfluidics have resulted in robust and high-throughput methods for micrometer-scale segregation. These techniques rely on external force fields (7, 8), sorting based on fluorescence (9), intricate separator geometries (10–18), or carriers with non-Newtonian behavior (19). An alternative approach toward microscale separation is to leverage the long-range hydrodynamic interactions emerging from fluid–structure coupling (20, 21). By tuning these interactions particle trajectory can be controlled, thus enabling separation (22).

A model system common in microfluidic applications, exhibiting such interactions, is confined Stokes flow in a Hele–Shaw cell. In it, particles or droplets are sandwiched between a pair of confining walls of a shallow microfluidic channel and are subjected to creeping flow (23). Owing to the shallowness of the cell, the flow is effectively two dimensional (2D) (24). What is more, the particle scatters the surrounding fluid, creating a dipolar flow disturbance, which decays with $1/r^2$, where r is the distance from the particle center. This flow disturbance strongly couples the particle to its surroundings. Experimentally, creating and driving particles in shallow channels have become widely accessible with the advent of microfluidics and soft lithography (25–31). Their easy fabrication and versatile out-of-equilibrium behavior make particles in confined Stokes flow an interesting toy system for the study of flow-mediated separation and self-assembly (32, 33).

Utilizing long-ranged hydrodynamic interactions (HIs), Beatus et al. (34, 35) demonstrated how trains of "pancake" droplets flow along a Hele–Shaw cell as out-of-equilibrium

one-dimensional crystals. In a similar experiment, Shen et al. (36) compare the dynamics of clusters comprising two or three droplets as they interact near or far away from the side walls of the cell. The presence of a side wall breaks the symmetry of the system and induces transversal motion of the cluster. Cross-streamline migration is also present if the symmetry of an individual particle, rather than that of an ensemble of particles, is reduced. A particle with two planes of mirror symmetry, such as a rod (37, 38) or a symmetric disk dimer (22), also moves toward one of the side walls of a Hele–Shaw cell, provided its long axis is neither normal nor parallel to the flow. As one such particle approaches the channel boundary, it begins to interact with its hydrodynamic image (39), the flow symmetry is reduced even further, and the particle begins to rotate. All three modes of motion, namely, rotation and streamwise and cross-streamwise translation, are also present when an asymmetric disk dimer is far away from any side walls as demonstrated by Uspal, Eral, and Doyle (22). Evidently, screened hydrodynamic interactions give rise to nontrivial behavior not only in particle ensembles (40–44), but also in single-particle systems with broken symmetry (45–51). A first step toward the development of low-cost flow separators requires understanding the relation between the geometry of one such particle and its trajectory in confined Stokes flow.

Significance

Particles of all shapes and sizes flowing through tight spaces are ever present in applications across length scales ranging from blood flow through tissue capillaries to industrial-scale processes. To date, separating these particles relies on methods employing external force fields. Currently underexplored, omnipresent fluid–structure interactions hold the key to shape-based separation independent of external intervention. By leveraging experiments, theory, and simulations, we show how the symmetry of a particle determines its overall trajectory: In particular, mirror-symmetric particles, both strongly and weakly confined, follow a universal path. We propose minimalistic scaling relations to describe how particle shape affects the parameterization of the universal path. These findings could be used to "program" particle trajectories in lab-on-a-chip devices and industrial separation processes.

APPLIED PHYSICAL SCIENCES

In this study, we combine theoretical and experimental approaches to investigate how particle shape can be tailored to induce self-steering under flow in quasi-2D microchannels. Controlling the motion of a particle in flow facilitates its separation. To this end, we use optical microscopy to track the in-plane motion of a variety of particles with a single mirror plane subjected to creeping flow in a shallow microfluidic channel. The mirror plane is perpendicular to the top and bottom walls of the channel and bisects the particle in two identical pieces (white dashes in Fig. 1 A–D). Through finite-element (FE) calculations we link the shape-dependent dynamics of the particles to the flow disturbances they create as they lag the far-field flow. Using Stokes linearity and the force-free nature of the particles, we collapse their reorientation and cross-streamwise dynamics onto two master curves. We accomplish this collapse by scaling each particle's angular and transversal velocities by two characteristic times. Finally, through minimalistic scaling relations we link these timescales to a particle's geometrical parameters including, but not limited to, area, moment of inertia, and length. Our scaling arguments predict the characteristic times from both experiments and FE computations up to a factor on the order of unity. This good agreement among experiments, simulations, and scaling arguments is a strong indication that the observed dynamics are universal to mirror-symmetric particles in quasi-2D Stokes flow.

To produce strongly confined polymeric particles with distinct shapes in a Hele–Shaw cell we use stop-flow lithography (SFL) (29), as depicted in Fig. 1 A–D. In a nutshell, SFL creates particles by projecting the image of a mask onto a photoreactive fluid. We choose dimeric and trimeric particles, composed of, respectively, two or three simple shapes connected by rigid shafts. The building blocks for dimers are disks, triangles, or squares (Fig. 1 B, D, and A), while those for trimers are always disks (Fig. 1C). For brevity, we denote disk, triangle, and square dimers with "D," "F," and "S," while "T" stands for trimers. In all cases one of the building blocks is larger with a size ratio $\kappa \equiv R_1/R_2$, where $1 < \kappa \leq 3$ and R_2 is the radius of the circle escribing the smaller shape. This asymmetry in the particle ensures its rotation even far away from any side walls (53). The trimers have an additional geometrical parameter, namely, the angle ϕ formed between the three disks (Fig. 1C). The vertex of ϕ is defined as the center of the larger disk, while the two rays starting from it point to the centers of the smaller equally sized disks. By changing ϕ we gain additional control over the dynamics of the particles (Fig. 1E). The geometry of the particle profoundly influences its trajectory: Particles with identical starting positions, yet slightly different geometries, follow dramatically different paths, as demonstrated numerically in Fig. 1E.

As the particles are created in situ, we directly track their motion in the viscous fluid by moving the stage of an optical microscope. We set the system in motion by applying a small pressure drop across the channel, thus inducing creeping flow with a Reynolds number $Re \sim 10^{-5}$. This flow regime, together with the large aspect ratio of the channel $W/H > 15$, allows us to average out the parabolic profile expected along the channel height H (Fig. 1F). Thus, the particle is effectively subjected to an in-plane potential flow with steep velocity gradients near the side walls of the channel and a constant velocity u for most of its width W (54) (Fig. 1G).

Apart from preventing sticking, the fluid layers with thickness h_g present above and below the particle strongly affect its motion (Fig. 1F and Fig. 1 F, Inset). As the particle moves along the channel with a longitudinal velocity $\dot{x}$, it experiences additional drag, because it shears the lubricating fluid in the gaps. To distinguish this drag from the drag due to the in-plane flow around the particle, we dub these two interactions "friction" and "flow" drag, respectively. Due to the strong particle confinement the velocity profile in the gaps is close to linear (38, 52), allowing us to assume Couette flow in the gaps (Fig. 1F). The friction drag from the confining walls F_x^w scales with $-2\dot{x}\eta/h_g$ and slows down the particle, where η is the dynamic viscosity of the fluid. Furthermore, it ensures the particle is confined to the plane of the flow, because any tilt or out-of-plane motion results in additional force acting on either face of the particle. Thus, the particle exhibits 3 degrees of freedom: translation along the length x and width y of the channel and in-plane rotation θ (Fig. 1G).

The particle lags the flow, perturbing the velocity field, and as a result pressure builds up on the upstream particle surface. This flow disturbance is strongly dependent on the particle shape (cf. Fig. 2 A and B). To illustrate this phenomenon, we use FE computations (52) to calculate the forces and torque acting on two distinctly shaped particles with $\kappa = 1.6$: a dimer and a trimer with $\phi = 120°$. We impose a unidirectional inlet flow with height-averaged velocity u and prescribe a longitudinal velocity $\dot{x} = u/2$ to each particle. We orient the particles in such a way that their mirror axes form an angle $\theta = 60°$ with the flow. The particle heights H_p in both cases are equal and comparable to the channel height H, with $H_p/H \sim 0.8$. While the longitudinal forces F_x acting on the two shapes are identical ($F_x^D/F_x^T = 0.99$),
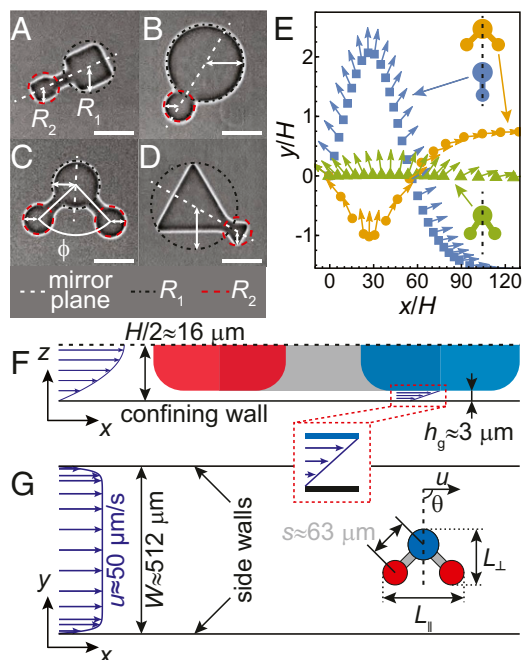

Fig. 1. Mirror-symmetric particles in quasi-2D Stokes flow. (*A*–*D*) Stop-flow lithography (29) produces strongly confined microparticles with various shapes in a Hele–Shaw cell. We investigate particles with a single mirror plane, each one consisting of two or three simple building blocks such as disks, squares, or triangles, connected with rigid shafts. These particles are a useful toy system to study how the geometry of a particle determines its trajectory. (*E*) We demonstrate this strong shape dependence by comparing the trajectories of three particles with $R_1/R_2 = 1.5$: from top to bottom a trimer with $\phi = 90°$ and a dimer and a trimer with $\phi = 68°$. The small arrows denote the orientation of the particles. The trajectories are obtained via 3D finite-element calculations. (*F*) We assume a planar Poiseuille profile along the height of the channel and Couette flow in the thin lubrication gaps with height h_g. Due to channel symmetry, we present only half of a Hele–Shaw cell with particle to scale and highlight the bottom confining wall. (*G*) Upon depth averaging, we arrive at the so-called Brinkman flow with steep velocity gradients near the side walls and constant velocity u along most of the channel width. In this top view the particle is magnified 2.5 times. The streamlines in all three flow profiles are represented by horizontal blue arrows. (Scale bars, 50 μm.)
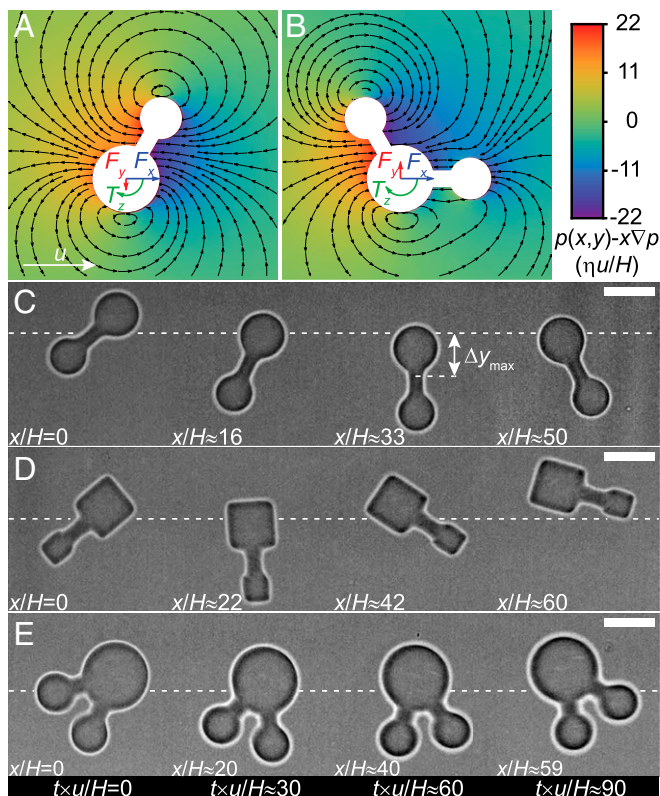
Fig. 2. (*A* and *B*) Particle-induced flow disturbances in a Hele–Shaw cell. As the particle thickness $H_p = H - 2h_g$ is comparable to the channel height $H_p/H \simeq 0.8$, the particle lags the surrounding flow, creating shape-specific velocity and pressure disturbances (cf. arrows and density plots in *A* and *B*). As the disturbances differ, so too do the hydrodynamic forces and torque acting on each particle differ. While the streamwise forces F_x on a dimer and a trimer have similar magnitudes (horizontal blue arrows), the drift forces F_y and torques T_z acting on them differ (vertical red arrows and clockwise green arcs, respectively). (*C*–*E*) This shape dependence of the forces and torque results in distinct linear and angular velocities, which manifest themselves in the different trajectories followed by different particles (cf. *C*, *D*, and *E*). The orientation and scaled position x/H as function of scaled time $t \times u/H$ are strongly dependent on particle shape. The disturbances to the pressure and velocity fields, as well as the forces and torques on the particles, are calculated using a 3D finite-element scheme (52). In all subfigures the flow is from left to right as denoted by the white arrow in *A*. (Scale bars, 50 μm.)

the torques differ—the dimer experiences a smaller torque $T_z^D/T_z^T = 0.81$. The difference in the transversal forces F_y is even more evident, as its direction also changes: $F_y^D/F_y^T = -0.67$. This disparity can be traced back to the pressure disturbance created by each particle—the larger the disturbance is, the larger the forces.

The shape dependence of the disturbances manifests itself in the distinct dynamics of different particles, as shown in Fig. 1*E*. To demonstrate this distinction experimentally, we compare the motion of three particles with different shapes, which have one and the same initial position and orientation, x/H, y/H, and $\theta_0 = 7\pi/9$, respectively (Fig. 2 *C–E*). While all three particles rotate to orient their larger building block upstream, only the dimers experience a significant lateral drift. Nagel et al. (38) report a similar coupling between longitudinal and transversal motion for symmetric rods, which drift at a constant velocity as they flow downstream. However, cross-streamwise motion is orientation dependent, resulting in a nonlinear cross-stream trajectory when an asymmetric dimer rotates: As our particles become perpendicular to the flow, their transversal velocities

diminish. Moreover, after acquiring this perpendicular orientation both particles change the direction of their lateral motion (cf. Fig. 2 *C*, *Center Right* and Fig. 2 *D*, *Center Left*). The coupling between rotation and translation explains why the disk dimer moves farther away from its initial position $\Delta y_{max}(t \times u/H = 60) \sim 1.5H$ compared to the square dimer, which covers half of that distance in half the time (cf. Fig. 2 *C*, *Center Right* and Fig. 2 *D*, *Center Left*). Due to its slower rotation, the disk dimer spends a longer time crossing streamlines before orienting perpendicular to the flow and starting to move in the opposite direction. This reasoning does not, however, answer the question of why the trimer experiences negligible drift, even though its rotational velocity is comparable to that of the disk dimer.

Understanding why these mirror-symmetric particles rotate in the absence of a side wall, while rod-like ones do not (38), requires introducing the concept of the center of hydrodynamic stress (CHS). First identified by Brenner (55), CHS is a point about which rotation is force-free and translational motion is torque-free in an unbounded fluid. However, as already mentioned, a confined particle moving in a flow experiences two types of drag. The friction drag can be considered to be applied at the particle centroid and the flow drag at the CHS. Both the CHS and the centroid of a mirror symmetric particle lie on the mirror plane. The latter, which indicates how area is distributed, is always closer to the larger of the two blocks composing an asymmetric dimer. Conversely, as the flow acts predominantly on the particle sides, it is the perimeter that affects the position of the CHS. The two points coincide for particles with an even number of mirror planes, thus canceling rotation. Any asymmetry, however, offsets the two points by a finite distance, placing the centroid closer to the larger building block. Then, the two types of drag acting on different geometric points produce a torque which rotates the particle toward an orientation in which the centroid, and by extension the larger component, is farther upstream. More detailed discussions of this concept are given in refs. 56 and 57.

Evidently, the observed coupling between the modes of translation and the rotation is a hallmark of flowing particles with low symmetry (58). However, there are three notable differences between particles in confined Stokes flow and the rods studied by Russel et al. (58), which sediment in three dimensions. Due to confinement, disturbances in quasi-2D flow decay faster than in three dimensions (3D): $1/r^2$ as opposed to $1/r$. The latter produces disturbances which are described with a series of coupled Stokeslets in contrast to the deformed dipoles we observe in quasi-2D. Finally, while sedimentation obeys the Galilean invariance principle, a confined particle moving with velocity $\dot{x} = u$ experiences a force due to the friction drag from the gaps. Surprisingly, despite these disparities, there is an intriguing similarity between the two systems. Particles in confined Stokes flow behave analogously to those driven by gravity in an unbounded fluid: Objects drift and rotate in opposite directions, depending on the driving mechanism. This phenomenon has been discussed by Uspal et al. (22) and is illustrated by Nagel et al. in ref. 38, figure 1. A possible explanation for these "mirrored" dynamics is the presence of two opposing forces acting on particles in both systems: During sedimentation viscous drag counteracts gravity, but is counteracted by friction drag when a particle is confined.

Mathematically, we represent the interdependence of particle degrees of freedom using a resistance tensor R_p, a symmetric matrix with size equal to the number of degrees of freedom a particle exhibits (*SI Appendix*, sections 1A and 1B). The resistance tensor relates the hydrodynamic forces and torque a stationary fluid $u = 0$ exerts on a particle, which translates through it with velocities $\dot{x}$ and $\dot{y}$, while also rotating at a rotational velocity $\dot{\theta}$ (55, 59):

$$\begin{pmatrix} F_x \\ F_y \\ T_z \end{pmatrix} = -\eta R_P \cdot \begin{pmatrix} \dot{x} \\ \dot{y} \\ \dot{\theta} \end{pmatrix}, \text{with } R_P \sim \begin{pmatrix} l_{xx} & l_{xy} & l_{x\theta}^2 \\ l_{yx} & l_{yy} & l_{y\theta}^2 \\ l_{\theta x}^2 & l_{\theta y}^2 & l_{\theta\theta}^3 \end{pmatrix}. \qquad \textbf{[1]}$$

We present each component of R_P in terms of arbitrary length scales l_{ij} to demonstrate one of its defining features—much like Stokes flow itself, the resistance tensor is time independent and defined purely by geometry. If the particle possesses only a single mirror plane, all nine components of R_P are generally nonzero, reflecting the entwined nature of its modes of motion (*SI Appendix*, section 1C). Conversely, for a rod the l_{ij}^2 components become zero, since its coupled translational modes are unaffected by rotation. Particles with an even higher symmetry such as disks have all three modes independent of each other and their resistance tensors are diagonal matrices.

Using the concept of the resistance tensor together with Stokes linearity, we recently derived equations of motion for a force-free mirror-symmetric particle subjected to confined Stokes flow (60). Briefly, being a linear transformation of velocity into force, the resistance tensor at angle θ can be rotated by $\Delta\theta$ about the z axis, yielding the resistance tensor at a new angle $\theta + \Delta\theta$: $R_P(\theta + \Delta\theta) = M_z(\Delta\theta) \cdot R_P(\theta) \cdot M_z^T(\Delta\theta)$. The rotation matrix $M_z(\Delta\theta)$ is detailed in *SI Appendix*, section 1A and Eq. **S3**. Alternatively, the particle velocity can be rotated by $-\Delta\theta$ using the same matrix. Applying a similar approach to the flow velocity and balancing the flow force acting on a stationary particle to the drag on a moving particle in a quiescent fluid we obtain a system of linear equations (*SI Appendix*, section 1B). Solving this system yields how particle orientation $\theta(t)$ and lateral displacement $y(t)$ change over time. Both equations, as presented in ref. 60, seemingly depend on the initial orientation of the particle θ_0. However, once we realize Stokes flow is time reversible, θ_0 becomes an arbitrary reference angle. For convenience, we set $\theta_0 = \pi/2$, resulting in

$$\theta(t) = 2 \arctan\left[\exp\left(-\frac{t - t_\perp}{\tau}\right)\right] \qquad \textbf{[2]}$$

and

$$y(t) = y(t_\perp) + 2H\frac{\tau}{\tau_y}\left[\text{sech}\left(\frac{t - t_\perp}{\tau}\right) - 1\right], \qquad \textbf{[3]}$$

where $t_\perp = t(\theta = \pi/2)$ denotes the time at which the particle is perpendicular to the flow. The two timescales, τ and τ_y, are characteristic for the reorientation and cross-stream migration of each particle. Numerically, they can be computed directly from the resistance tensor (60), and just like R_P, they are purely geometrically determined. Furthermore, Eq. **3** captures the coupling between rotation and translation, because the particle path depends on both timescales. The generality of these equations of motion points to their validity for a wide range of particle shapes provided they have at least one plane of mirror symmetry. The equations also hold for particles that do not rotate—shapes with more than one mirror plane have an infinitely large τ and translate at a constant lateral velocity (*SI Appendix*, section 1C).

To test the validity of these equations, we produce a variety of disk dimers and track their motion as they rotate from $\theta \sim 0.85\pi$ to $\theta \sim 0.10\pi$. Upon comparing the obtained raw experimental trajectories, we see a qualitative similarity (*SI Appendix*, Fig. S4). However, as some particles rotate more slowly than others, the overall paths the particles follow differ considerably in quantitative terms. We fit Eqs. **2** and **3** to the observed trajectories and extract the two characteristic times for each particle, as discussed in *SI Appendix*, section 2. Finally, we transform experimental time to $(t - t_\perp)/\tau$ for each shape and compare the angle evolution for the set of dimers (top curve in Fig. 3*A*). The reorientation dynamics of the studied disk dimers do not only

agree quantitatively—they seem to be independent of the exact particle shape as evident from the collapsed experimental data, which closely follows Eq. **2**, as well as 3D FE computations. This apparent shape independence implies that the characteristic time captures all geometric details of a particle. By condensing them in τ and factoring them out, we are left with the general dynamics determined by the mirror symmetry and described well by our equation for $\theta(t)$. This notion is reaffirmed once we take a look at the lateral motion of the disk dimers (bottom curve in Fig. 3*A*). Their cross-streamwise motion also appears shape independent once we use $(t - t_\perp)/\tau$ instead of experimental time and scale their lateral displacement by the channel height and the characteristic times. Even when the lateral motion of a particle deviates from the one predicted by Eq. **3**, the deviation can be traced back to the reorientation dynamics. Some dimers stop rotating before their mirror axes align with the flow direction, leading to a decoupling of rotation and translation. Thus, they begin to behave as rods with a finite cross-stream velocity even at long timescales (38). A possible reason for these deviations is interaction with hydrodynamic images if the particle comes too close to the wall. Additionally, artifacts of the lithography process such as slight asymmetry in the particle itself or dust of size comparable to h_g are other possible culprits. We test these notions by simulating the full trajectory of a dimer whose experimental behavior deviates from the theoretically predicted one. Since the 3D FE results are well described by the equations of motion and agree with the experimental trajectories, we conclude that the observed deviations are indeed experimental artifacts.

Encouraged by the close agreement between theory and experiments in Fig. 3*A*, we broaden our scope to mirror symmetric particles of various shape. Substituting the disks with pointy building blocks such as squares and triangles leads to different timescales, but does not affect the general particle dynamics (Fig. 3*B*). Increasing the number of building blocks has the same effect—trimers with different size ratios and interdisk angle also behave identically once we isolate the geometrical details condensed in τ and τ_y. This universality, remarkable as it is, is not entirely unexpected—Eqs. **2** and **3** are derived with the sole assumptions of a force- and torque-free particle with a mirror plane moving in creeping flow. Moreover, our findings suggest we should expect this type of dynamics from any particle that has at least one mirror plane and is subjected to confined Stokes flow. Our reasoning also raises the question, What is the behavior of an asymmetric particle, for instance, a trimer where all three disks have different radii (*SI Appendix*, Fig. S3)? One such shape rotates until it acquires a stable orientation $\theta_\infty \neq 0$ as discussed in *SI Appendix*, section 1C. However, since the flow disturbance it creates is asymmetric, the particle has a nonzero lateral velocity even after it has ceased reorienting (48, 60). Finally, the assumption of heavy confinement ($H_p/H > 0.8$) does not preclude applying our general approach to less-confined particles, since rods spanning half the channel height also experience measurable cross-stream motion (38). Also, a thin mirror-symmetric particle ($H_p/H = 0.5$) and its strongly confined counterpart (i.e., a particle having the same in-plane shape but larger H_p/H) follow identical paths, as shown numerically in Fig. 3*A*. Similarly, this universality is not restricted to particles with uniform thickness: A spherical dumbbell, comprising two unequal spheres and a cylinder, also follows the universal trajectory (Fig. 3*B*). While the larger, strongly confined, sphere has a radius of $0.4H$, the smaller one spans only half the channel height and the connecting cylinder has a radius of $0.15H$.

Although we have a rigorous description of the general trajectory of a mirror-symmetric particle, its exact motion still depends on two timescales. Up to now we obtain τ and τ_y as fitting parameters in Eqs. **2** and **3**. However, knowing their values a priori opens the door toward tailoring the shape of a particle
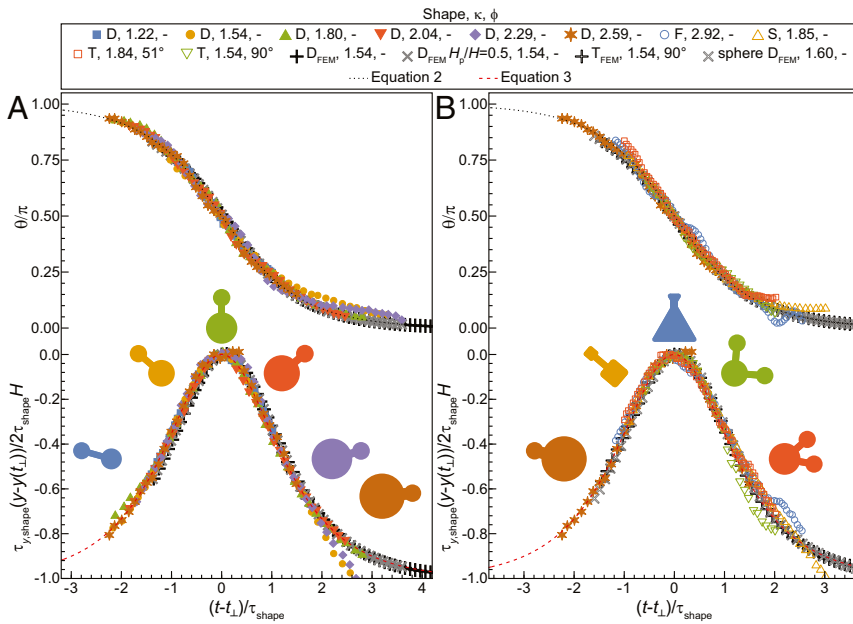
Fig. 3. (*A* and *B*) Universal motion of mirror-symmetric particles. Regardless of their detailed shape, all studied particles follow a universal trajectory. They exhibit the same quantitative behavior as long as we take into account two characteristic times, τ and τ_y, scaling their modes of motion (52): exponentially decaying rotation $\theta(t)$ to orient with the big disk upstream (top curves) and bell-shaped translation in the lateral direction $y(t) - y(t_\perp)$ (bottom curves). The only geometrical element common to all studied particles is their single plane of mirror symmetry. In all cases, the error bars denoting experimental uncertainty are smaller than the symbols and are omitted. The particles and their motion are sketched in the middle. In the key disk, square, and triangle dimers are denoted with D, S, and F for brevity. Disk trimers are denoted as T. Angles, where given, are for the trimer angle ϕ defined in Fig. 1*C*. The subscript "FEM" signifies that some trajectories are obtained through our finite-element scheme. We also demonstrate that this type of motion is present even at weaker confinement ($H_p/H < 0.8$) and is not limited to objects with constant thickness: A particle spanning half the channel height (D_{FEM} $H_p/H = 0.5$, 1.54, −) and a particle comprising two unequal spheres held together by a rigid cylinder (sphere D_{FEM}, 1.60, −) follow the same universal path.

to a desired trajectory. One possible way to obtain this target-specific shape is to survey a large variety of particles, compute their resistance tensors, and estimate τ and τ_y (60). As robust as this method is, it is not particularly insightful as it does not yield an explicit relation between the timescales and a particle's geometric parameters. By considering imbalanced rods, we propose scaling arguments linking the timescales τ and τ_y of a particle to its geometry.

We do so by first taking the time derivatives of θ and y in Eqs. **2** and **3** and substituting $(t - t_\perp)/\tau = -\ln(\tan(\theta/2))$ in the resulting expressions. This yields $\dot{\theta} = -\sin\theta/\tau$ and $\dot{y} = -2H\sin\theta\cos\theta/\tau_y$, respectively. The former expression points to an inverse relation between the rotational timescale and the rotational velocity when the particle is parallel to the flow: $\tau_{scaling} = 1/\dot{\theta}(\theta = -\pi/2)$. We avoid the angular dependence in the latter derivative by using a similar expression for the drift velocity of rods used by Nagel et al. (38): $\dot{y}_{rod} = -(\dot{x}_\perp - \dot{x}_\parallel)\sin\theta\cos\theta$. The subscripts of the streamwise velocities denote particle orientation: $\dot{x}_\perp = \dot{x}(\theta = \pi/2)$ and $\dot{x}_\parallel = \dot{x}(\theta = 0)$. Since rods are a special case of mirror-symmetric particles, rather than a separate class, we assume $\dot{y}_{rod} = \dot{y}$ and demonstrate the assumption's validity in *SI Appendix*, Fig. S16*C*. Finally, we express τ_y via the difference in the longitudinal velocities when the particle is perpendicular and parallel to the flow: $\tau_{y,scaling} = 2H/(\dot{x}_\perp - \dot{x}_\parallel)$.

To compute the three velocities, we make use of the force- and torque-free nature of the particle. At any instant in time, the angular momentum it gains from the in-plane flow is dissipated as Couette torque from the confining walls above and below its faces: $T_z^f + T_z^w = 0$. We write two similar balances for the streamwise force—the friction from the confining walls and the drag from the surrounding fluid cancel: $F_{x,i}^w + F_{x,i}^f = 0$, where the subscript i in the x components of the force denotes particle orientation. We express $F_{x,i}^w$ by integrating the hydrodynamic stress from the Couette flow in the gaps over the particle faces with area S_p: $F_{x,i}^w \sim -2\eta\dot{x}_i S_p/h_g$. We neglect any rotational contribution from the force because the particle does not rotate at $\theta = 0$ and even when it does at $\theta = \pm\pi/2$, the coupling between the two modes of motion is weak. We use a similar approach to calculate the Couette torque acting on the two faces of a rotating particle: $T_z^w \sim -2\eta\dot{\theta}/h_g \int_{S_p}(r - c_0)^2 dS_p = -2\eta\dot{\theta}I_p/h_g$, where r are the coordinates of all differential area elements dS_p and we

identify the integral as the area moment of inertia I_p. By computing the wall torque with respect to the particle centroid c_0, we decouple streamwise motion from rotation.

To estimate $F_{x,i}^f$, we follow the approach of Beatus et al. (35) and assume the flow force acting on the particle is dominated by the fluid pressure. While this is a good approximation when the particles are oriented normal to the flow, $F^{visc}/F^{press} \sim (2H/L_\perp)^2 \lesssim 1/4$, when $\theta = 0$, the force ratio is $(2H/L_\parallel)^2 \sim 1$. The projected lengths L_i are sketched in Figs. 1*G* and 4*C*. Making this strong assumption ultimately leads to an underestimation of τ_y. Next, we integrate the pressure difference across the width of the particle $-\Delta x(y)\partial p/\partial x$ along its surface normal to the flow $H_p L_i$ and obtain

$$F_{x,i}^f \sim -\frac{\partial p}{\partial x} H_p \int_{L_i} \Delta x(y)dy \sim \frac{12\eta u}{H^2} \times H_p \times L_i\sqrt{\frac{S_p}{\pi}}\frac{L_\parallel}{L_\perp}, \quad [4]$$

where we express the far-field pressure gradient $-\partial p/\partial x = 12\eta u/H^2$ through the depth-averaged flow velocity u. Additionally, we substitute the integral of the width Δx with the geometrically averaged width $\sqrt{S_p/\pi}L_\parallel/L_\perp$, which is computed as the radius of a circle with the same area scaled with the aspect ratio of the particle. Setting $F_{x,i}^f + F_{x,i}^w = 0$, we obtain an expression for the streamwise velocity: $\dot{x}_i \sim 6\tilde{h}H_p \times L_\parallel L_i/(L_\perp\sqrt{\pi S_p}) \times u/H$, where $\tilde{h} = h_g/H$.

Estimating the torque exerted by the flow on the particle requires integrating a differential contribution over each point on the particle sides. Alternatively, we can apply the pressure force $F_{x,\perp}^f$ at the center of hydrodynamic stress, which also produces a torque. As already discussed, the CHS is related to the perimeter of the 2D projection of the particle, because the flow acts predominantly on the particle sides. Then, we assume that, to a first approximation, the CHS coincides with the center of perimeter $c_p = P_p^{-1}\int_{P_p} r_p dP_p$, which results in the compact expression for the flow torque: $T_z^f \simeq |c_p - c_0| F_{x,\perp}^f = r_{arm}F_{x,\perp}^f$. We can then isolate the rotational velocity of the particle when it is perpendicular to the flow from the torque balance: $\dot{\theta} \simeq 6\tilde{h}H_p \times (r_{arm}L_\parallel\sqrt{S_p/\pi})/I_p \times u/H$. A
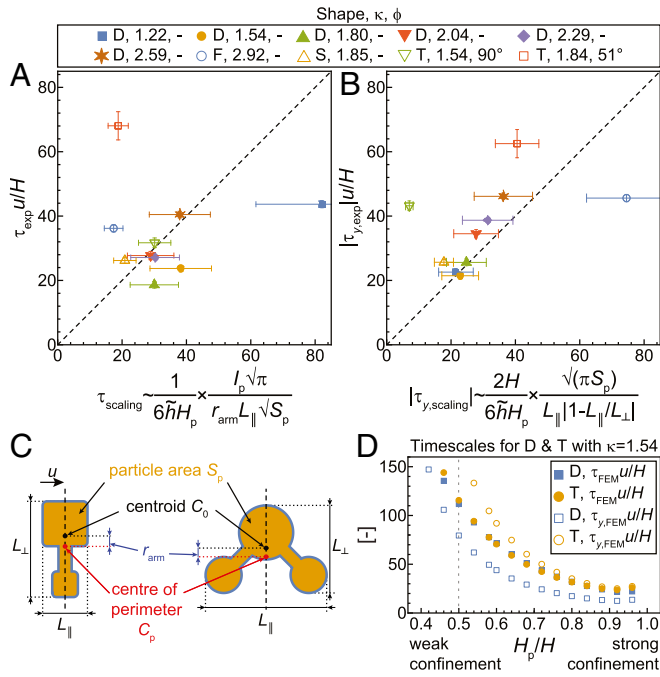
Fig. 4. Relation of the characteristic timescales to particle geometry. The (*A*) rotation and (*B*) translation timescales needed to fully describe particle motion via Eqs. **2** and **3** are solely dependent on the geometry of the system. For identical flow parameters such as depth-averaged flow velocity u, gap thickness h_g, and channel height H, the detailed shape of the particle determines τ and τ_y. The rotational timescale depends on the area of the particle S_p, its projected length when perpendicular to the flow $L_\perp$, and the distance $r_{arm} = |c_p - c_0|$ spanning from the centroid $c_0 = S_p^{-1} \int_{S_p} r dS_p$ to the center of perimeter $c_p = P_p^{-1} \int_{P_p} r_p dP_p$, where r are the coordinates of the differential area elements dS_p and r_p are points on the particle perimeter P_p. Additionally, we need the area moment of inertia $I_p = \int_{S_p} (r - c_0)^2 dS_p$. We obtain the translational timescale via the area of the particle and its projected lengths $L_\perp$ and $L_\parallel$ when its mirror plane is perpendicular or parallel to the flow, respectively. The vertical error bars represent the SD of the timescales within an experimental series (*SI Appendix*, Table S1). The horizontal error bars are calculated from the uncertainty of the gap thickness $h_g = 2.5 \pm 0.5$ μm. The dashed diagonal lines with a slope of unity are a guide to the eye and serve to assess the agreement between the experimental results and scaling relations. All particle shape parameters needed to estimate τ and τ_y are sketched in *C*. As the height of the particles H_p is reduced, their timescales begin to diverge, as shown numerically in *D*. Yet particles spanning half the channel height still exhibit a measurable cross-stream and rotational motion (gray dashed line).

detailed version of these derivations can be found in *SI Appendix, section 1E*.

Finally, we substitute the three velocities in the expressions for the two timescales and arrive at our minimalistic scaling relations for τ and τ_y:

$$\tau_{\text{scaling}} \simeq \frac{1}{6\tilde{h}H_p} \times \frac{H}{u} \times \frac{\sqrt{\pi}I_p}{r_{arm}L_\parallel \sqrt{S_p}} \qquad [5]$$

and

$$\tau_{y,\text{scaling}} \simeq 2H \times \frac{1}{6\tilde{h}H_p} \times \frac{H}{u} \times \frac{\sqrt{\pi S_p}}{L_\perp - L_\parallel} \frac{L_\perp}{L_\parallel}. \qquad [6]$$

The geometrical parameters that enter the two expressions are illustrated in Fig. 4*C* and detailed in the legend.

We verify the scaling models by comparing our experimental timescales to the ones computed via Eqs. **5** and **6** in Fig. 4 *A* and *B*. We complement this comparison with numerical timescales, computed via 3D FE method, and present them in *SI Appendix,*

Figs. S18 and S19. The scaling relation for τ_{scaling} overestimates some τ_{exp} by a factor of roughly 1.6, while $\tau_{y,\text{scaling}}$ underestimates the majority of $\tau_{y,\text{exp}}$ by a factor $\sim$1.5. This mismatch is to be expected as the proposed minimalistic scalings strip the particles of any geometric detail.

Although we determine the two timescales up to a scaling factor of order 1, Eqs. **5** and **6** accurately predict when τ or τ_y diverges and when τ_y becomes negative. In some trivial cases, particles cease to rotate and $\tau \to \infty$ when there is no flow ($u \to 0$), they are either too thick ($\tilde{h} \to 0$) or too thin ($H_p \to 0$). The latter effect is demonstrated numerically in Fig. 4*D*. The timescale also diverges when the distance between the centroid and the center of perimeter vanishes ($r_{arm} \to 0$). Particles with more than one mirror plane—rods, symmetric dimers, and disks—all have $r_{arm} = 0$. Similarly, particles do not cross streamlines when their two projected lengths match $L_\perp = L_\parallel$. One such particle is a trimer with $\kappa = 1.5$ and $\phi \sim 68°$, which rotates without drifting away from the centerline of the channel, as demonstrated by FE computations in Fig. 1*E*. We also observe this phenomenon experimentally: The trimer with $\kappa = 1.84$ and $\phi = 51°$ barely moves in the lateral direction (Fig. 2*E*). Its large τ_y, damping its lateral motion, is due to its comparable projected lengths. Furthermore, τ_y may become negative for trimers with large ϕ, as demonstrated in Fig. 1*E*. This change in drift direction is present experimentally for a trimer with $\kappa = 1.5$ and $\phi = 90°$ and is the reason why we compare $|\tau_{y,\text{exp}}|$ to $|\tau_{y,\text{scaling}}|$ in Fig. 4*B*.

The universal path we discovered renders separation of quasi-2D particles with at least one mirror seemingly impossible. However, estimating the two geometry-dependent timescales that govern the exact dynamics facilitates segregation by shape via careful separator design.

Since hydrodynamic interactions couple every object in flow to its neighbors, it is advisable to separate the mixture one particle at a time. Using a narrow inlet, a single object can be injected through the side wall of a channel filled with a stationary fluid. Then, another inlet, which is aligned with the channel side walls, sets the fluid and the particle in motion. The side inlet, which determines the initial orientation of the particle, should not be perpendicular to the walls to ensure cross-stream motion for particles with two mirror planes. Sequencing and balancing the strengths of these inlets can be done with a programmable microfluidic pump. This workaround comes at the expense of throughput, which can be amended by massive parallelism, a technique well suited for affordable and easy-to-fabricate microfluidic devices.

Next, we can use the symmetry of the particle to determine where it is most likely to be after a sufficiently long time. Asymmetric disk dimers with a single mirror plane focus to the centerline of the channel (22). In contrast, particles with two and zero mirror planes oscillate between the side walls (22, 38, 60), "hop" close to one of them (22, 38), or are captured by them (48). These distinct types of long-time behavior already hint at possible ways to separate particles based on their symmetry. Objects with a single mirror plane can be collected at the downstream outlet of the microfluidic device. Conversely, those with two or zero can be separated via strategically placed outlets at the sides of the channel.

In more general terms, depending on how quickly particles approach the wall relative to how quickly they rotate, we can discern two separation strategies: collecting them at the downstream outlet if $W/L_\perp \times \tau_y/\tau > 1$ and collecting them via side outlets otherwise. Additionally, we may use τ_y and W/H to estimate where to position the side outlets. A possible approach to separate particles with a single mirror plane based on asymmetry is to form a cascade of separators. In such a setup, particles collected at the main outlet of a channel are fed into the side inlet of a similar separator with a smaller W. A particle, which

previously migrated far from the side walls, may now, if only weakly asymmetric, remain in close proximity with a side wall, depending on the streamwise length of the cascade stage. Hence, estimating the timescales over which the symmetry-specific dynamics occur enables optimizing the geometry of a separator.

As a demonstration, we estimate τ and τ_y for different microplastic pollutants (figure 2 in ref. 61, figure 3 in ref. 62, and ref. 63). We carry out the same estimation for healthy and cancerous mammary cells from a mouse (figure 2 in ref. 4), where we make the common assumption that cells do not change shape due to flow (64). Throughout this discussion, we assume strong confinement for all objects, $H_{\mathrm{p}}/H = 0.8$. Microplastic pollutants differ vastly in shape: from straight slender fibers through asymmetric fragments through microbeads. Estimating the timescales governing the motion of fibers is particularly valuable as they are found in laundry machine effluents (63). Such slender rods have an aspect ratio close to zero ($L_\parallel/L_\perp < 0.05$) and their area in quasi-2D is approximately the product of their projected lengths: $S_{\mathrm{p}} \approx L_\parallel L_\perp$. We can then simplify Eq. 6 to $\tau_y u/H \simeq 2H\sqrt{\pi L_\perp/L_\parallel}/\left(6\tilde{h}H_{\mathrm{p}}\right)$. We anticipate large rotational timescales for the straight fibers and microbeads with $\tau > 1{,}000H/u$. While the latter should not exhibit any measurable cross-stream motion ($\tau_y > 1{,}000H/u$), the fibers should move from one side wall to another with $30 < \tau_y u/H < 80$. Asymmetric fragments should rotate but their rotational speed is strongly dependent on asymmetry. For the fragment shown in figure 2 of ref. 61, we estimate $\tau \sim 200H/u$ and $\tau_y \sim 20H/u$, where we assume the thickness of the particle $H_{\mathrm{p}} \sim 100$ μm is the same as its width. Similarly, it may be possible to separate cells based on their shape: Healthy mammary cells have a nearly rectangular shape ($\tau > 1{,}000H/u$) with aspect ratio between $1/2$ and $1/3$ ($\tau_y \approx 20H/u$). In stark contrast, tumor cells are close to circular, should not rotate, and should exhibit large $\tau_y > 200H/u$.

The applicability of the proposed scaling relations to a wide range of particles with different geometry and symmetry supports the main conclusion of our work: In confined Stokes flow, particles with at least one mirror plane behave identically as long as we scale their trajectories by characteristic times, directly related to their shape. The observed universal path can be utilized to predict trajectories of particles based on minimalistic scaling arguments.

Conclusion

In summary, by combining experiments, simulations, and theory, we investigate how the trajectory of both weakly and strongly confined particles subjected to Stokes flow is determined by their geometry. We observe that particles with a single mirror plane exhibit qualitatively similar behavior: They rotate in plane to align their mirror axis with the flow and their larger building block upstream, all of the while crossing streamlines. However, the timescales over which these dynamics happen are strongly dependent on particle shape. We fit our experimental trajectories and finite-element calculations to theoretical equations of motion we recently reported, thus extracting characteristic rotational and translational times for each particle. By scaling experimental time by the respective rotational timescale for each experiment, we collapse the evolution of the orientation for all particles onto a single curve. Similarly, we obtain a universal bell-shaped path by scaling real time and a particle's cross-streamline displacement. Finally, we propose minimalistic scaling relations linking the characteristic times of a particle to its geometry. We strip the particles of all geometrical details and treat them as imbalanced rods, thus reinforcing the idea that it is solely their symmetry that defines their overall dynamics. Our observations suggest the trajectories are universal for particles with at least one mirror plane. This finding deepens our understanding of fluid–structure interactions in confined Stokes

flow. Moreover, it opens additional opportunities in lab-on-chip and industrial applications enabling shape-based separation of suspended particles solely through hydrodynamic interactions.

Materials and Methods

Experimental Setup. Polymeric microparticles are produced and observed with an experimental setup, similar to the one used by Uspal, Eral, and Doyle (22). Polydimethylsiloxane (PDMS) (Sylgard 184; Dow Corning) microfluidic devices of width $W = 512 \pm 2$ μm are fabricated according to Dendukuri et al. (65). Disk dimers are tracked in channels with height $H = 30 \pm 1$ μm. Trimers and triangle and square dimers are tracked in 33-μm high channels. A UV-cross-linking oligomer, poly-(ethyleneglycol) diacrylate (PEG-DA) ($M_n = 700$, $\eta = 95$ mPa·s; Sigma-Aldrich), is mixed with a photoinitiator, hydroxy-2-methylpropiophenone (Darocur 1173; Sigma-Aldrich), in a 19:1 volume ratio and the mixture is pumped through the microfluidic channel. The device, loaded with prepolymer, is mounted on the stage of a motorized Nikon Ti Eclipse inverted optical microscope. A photolithographic mask with well-defined shape is inserted as a field stop. Mask designs are made in Wolfram Mathematica and postprocessed in Dassault Systèmes' DraftSight.

Particle Production and Tracking. Microparticles are produced by shining a 100-ms pulse of UV light through the mask onto the channel, thus confining photopolymerization to a discrete part of the prepolymer mixture. Oxygen, diffusing through the permeable PDMS walls of the device, inhibits polymerization in their vicinity (65). This facilitates the formation of two thin lubrication layers, $h_{\mathrm{g}} = 2.5 \pm 0.5$ μm, which separate the particles from the confining walls of the channel. Particles are produced and observed with a 20× lens. The microparticle is set in motion by applying a pressure drop $\Delta p \approx 1.5$ kPa across the channel, resulting in a depth-average flow velocity $u = 55$ μm·s^{-1} for the shallower channel and $u = 70$ μm·s^{-1} for the 33-μm high channel. The particle is tracked by moving the automated microscope stage in a stepwise manner.

The positions and orientations of particles containing disks are extracted from the acquired time series using a custom-written MATLAB script, which employs circular Hough transforms to identify the particle shape in each frame. The script utilizes MATLAB's Bio-Formats package (66) and the calcCircle tool. Particles comprising triangles and squares are tracked by fitting an ellipse to them, calculating the angle, and detecting their straight edges.

Finite-Element Computations. All computational results are obtained through the finite-element method as implemented in the Creeping Flow module of COMSOL Multiphysics 5.3, which we couple to MATLAB via LiveLink. Each solution is carried out on a single computational node fitted with an Intel Xeon E5-2620 v4 @ 2.10 GHz CPU and 64 GB memory. Technical details regarding geometry building, meshing, and solver settings are given in *SI Appendix*, section 3 (67–69).

We use the channel height $H = 1$ as a length scale. We set the inlet flow velocity u, the kinematic viscosity of the fluid η, and its mass density ρ to unity. To simulate creeping flow at this $Re = 1$, we neglect the inertial term in the momentum equation and solve the Stokes equation with no external forcing,

$$\nabla \cdot \left(-pI + \eta\left(\nabla \boldsymbol{U}_{\mathrm{f}} + \nabla \boldsymbol{U}_{\mathrm{f}}^{\mathrm{T}}\right)\right) = 0$$

$$\nabla \cdot \boldsymbol{U}_{\mathrm{f}} = 0,$$

where we solve for $\boldsymbol{U}_{\mathrm{f}}$ and p, the fluid velocity and pressure fields. We integrate the total stress over the particle surface to obtain the forces and torque acting on it at a given position and orientation with respect to the flow. To compute the force- and torque-free velocities of the particle at this configuration, we numerically solve the force balance

$$\begin{pmatrix} \dot{x} \\ \dot{y} \\ \dot{\theta} \end{pmatrix} = \frac{1}{\eta} R_{\mathrm{p}}^{-1} \cdot \boldsymbol{F}_0,$$

where $\boldsymbol{F}_0$ is the forces and torque acting on a stationary particle in a flow and R_{p} is the resistance tensor for this configuration (*SI Appendix*, section 1A and Eq. S1). We obtain the trajectory of a particle through a first-order time integration scheme, where we apply $\left(\dot{x}, \dot{y}, \dot{\theta}\right)$ over a timestep t_{step}, which we determine every iteration (*SI Appendix*, section 3).

Data Availability. Experimental data, theoretical derivations, and computational protocols that support the findings of this study are shown in this article and *SI Appendix*.

1. J. Bauer et al., Ritonavir: An extraordinary example of conformational polymorphism. *Pharm. Res.* **18**, 859–866 (2001).

2. A. R. Shet, S. Bates, F. X. Muller, D. J. Grant, Polymorphism in piroxicam. *Crys. Growth Des.* **4**, 1091–1098 (2004).

3. M. Piel, P. T. Tran, Cell shape and cell division in fission yeast. *Curr. Biol.* **19**, R823–R827 (2009).

4. M. B. Ginzberg, R. Kafri, M. Kirschner, On being the right (cell) size. *Science* **348**, 1245075 (2015).

5. R. Thompson et al., New directions in plastic debris. *Science* **310**, 1117b (2005).

6. M. L. Taylor, C. Gwinnett, L. F. Robinson, L. C. Woodall, Plastic microfibre ingestion by deep-sea organisms. *Sci. Rep.* **6**, 33997 (2016).

7. X. Ding et al., Cell separation using tilted-angle standing surface acoustic waves. *Proc. Natl. Acad. Sci. U.S.A.* **111**, 12992–12997 (2014).

8. A. Lenshof, T. Laurell, Continuous separation of cells and particles in microfluidic systems. *Chem. Soc. Rev.* **39**, 1203–1217 (2010).

9. P. L. Mage et al., Shape-based separation of synthetic microparticles. *Nat. Mater.* **18**, 82–89 (2019).

10. N. Nivedita, I. Papautsky, Continuous separation of blood cells in spiral microfluidic devices. *Biomicrofluidics* **7**, 054101 (2013).

11. J. Son, R. Samuel, B. K. Gale, D. T. Carrell, J. M. Hotaling, Separation of sperm cells from samples containing high concentrations of white blood cells using a spiral channel. *Biomicrofluidics* **11**, 054106 (2017).

12. J. Kim et al., Inertial focusing in non-rectangular cross-section microchannels and manipulation of accessible focusing positions. *Lab Chip* **16**, 992–1001 (2016).

13. D. Jiang, D. Huang, G. Zhao, W. Tang, N. Xiang, Numerical simulation of particle migration in different contraction–expansion ratio microchannels. *Microfluid. Nanofluidics* **23**, 7 (2019).

14. B. Behdani et al., Shape-based separation of micro-/nanoparticles in liquid phases. *Biomicrofluidics* **12**, 051503 (2018).

15. M. Li, H. E. Muñoz, K. Goda, D. Di Carlo, Shape-based separation of microalga Euglena gracilis using inertial microfluidics. *Sci. Rep.* **7**, 10802 (2017).

16. A. Russom et al., Differential inertial focusing of particles in curved low-aspect-ratio microchannels. *New J. Phys.* **11**, 075025 (2009).

17. A. J. Mach, J. H. Kim, A. Arshi, SC. Hur, D. Di Carlo, Automated cellular sample preparation using a Centrifuge-on-a-Chip. *Lab Chip* **11**, 2827–2834 (2011).

18. L. R. Huang, E. C. Cox, R. H. Austin, J. C. Sturm, Continuous particle separation through deterministic lateral displacement. *Science* **304**, 987–990 (2004).

19. M. A. Raoufi et al., Experimental and numerical study of elasto-inertial focusing in straight channels. *Biomicrofluidics* **13**, 034103 (2019).

20. S. C. Hur, S. E. Choi, S. Kwon, D. D. Carlo, Inertial focusing of non-spherical microparticles. *Appl. Phys. Lett.* **99**, 044101 (2011).

21. M. Masaeli et al., Continuous inertial focusing and separation of particles by shape. *Phys. Rev. X* **2**, 31017 (2012).

22. W. E. Uspal, H. B. Eral, P. S. Doyle, Engineering particle trajectories in microfluidic flows using particle shape. *Nat. Commun.* **4**, 2666 (2013).

23. T. Beatus, I. Shani, R. H. Bar-Ziv, T. Tlusty, Two-dimensional flow of driven particles: A microfluidic pathway to the non-equilibrium frontier. *Chem. Soc. Rev.* **46**, 5620–5646 (2017).

24. G. K. Batchelor, "Flow of a uniform incompressible viscous fluid" in *An Introduction to Fluid Dynamics* (Cambridge University Press, 2000), pp. 174–263.

25. S. Y. Teh, R. Lin, L. H. Hung, A. P. Lee, Droplet microfluidics. *Lab Chip* **8**, 198–220 (2008).

26. P. Zhu, L. Wang, Passive and active droplet generation with microfluidics: A review. *Lab Chip* **17**, 34–75 (2017).

27. L. Shang, Y. Cheng, Y. Zhao, Emerging droplet microfluidics. *Chem. Rev.* **117**, 7964–8040 (2017).

28. D. Dendukuri, D. C. Pregibon, J. Collins, T. A. Hatton, P. S. Doyle, Continuous-flow lithography for high-throughput microparticle synthesis. *Nat. Mater.* **5**, 365–369 (2006).

29. D. Dendukuri, S. S. Gu, D. C. Pregibon, T. A. Hatton, P. S. Doyle, Stop-flow lithography in a microfluidic device. *Lab Chip* **7**, 818–828 (2007).

30. D. Dendukuri, P. S. Doyle, The synthesis and assembly of polymeric microparticles using microfluidics. *Adv. Mater.* **21**, 4071–4086 (2009).

31. S. E. Chung et al., Optofluidic maskless lithography system for real-time synthesis of photopolymerized microstructures in microfluidic channels. *Appl. Phys. Lett.* **91**, 17–20 (2007).

32. Z. Ge, O. Tammisola, L. Brandt, Flow-assisted droplet assembly in a 3D microfluidic channel. *Soft Matter* **15**, 3451–3460 (2019).

33. W. E. Uspal, P. S. Doyle, Self-organizing microfluidic crystals. *Soft Matter* **10**, 5177–5191 (2014).

34. T. Beatus, T. Tlusty, R. Bar-Ziv, Phonons in a one-dimensional microfluidic crystal. *Nat. Phys.* **2**, 743–748 (2006).

35. T. Beatus, R. H. Bar-Ziv, T. Tlusty, The physics of 2D microfluidic droplet ensembles. *Phys. Rep.* **516**, 103–145 (2012).

36. B. Shen, M. Leman, M. Reyssat, P. Tabeling, Dynamics of a small number of droplets in microfluidic Hele–Shaw cells. *Exp. Fluids* **55**, 1728 (2014).

37. H. Berthet, M. Fermigier, A. Lindner, Single fiber transport in a confined channel: Microfluidic experiments and numerical study. *Phys. Fluids* **25**, 103601 (2013).

38. M. Nagel et al., Oscillations of confined fibres transported in microchannels. *J. Fluid Mech.* **835**, 444–470 (2018).

39. W. E. Uspal, P. S. Doyle, Scattering and nonlinear bound states of hydrodynamically coupled particles in a narrow channel. *Phys. Rev. E* **85**, 016325 (2012).

40. T. M. Schneider, S. Mandre, M. P. Brenner, Algorithm for a microfluidic assembly line. *Phys. Rev. Lett.* **106**, 094503 (2011).

41. Y. Green, Approximate solutions to droplet dynamics in Hele-Shaw flows. *J. Fluid Mech.* **853**, 253–270 (2018).

42. B. Cui, H. Diamant, B. Lin, Screened hydrodynamic interaction in a narrow channel. *Phys. Rev. Lett.* **89**, 188302 (2002).

43. U. D. Schiller, J. B. Fleury, R. Seemann, G. Gompper, Collective waves in dense and confined microfluidic droplet arrays. *Soft Matter* **11**, 5850–5861 (2015).

44. I. Shani, T. Beatus, R. H. Bar-Ziv, T. Tlusty, Long-range orientational order in two-dimensional microfluidic dipoles. *Nat. Phys.* **10**, 140–144 (2014).

45. O. du Roure, A. Lindner, E. N. Nazockdast, M. J. Shelley, Dynamics of flexible fibers in viscous flows. *Annu. Rev. Fluid Mech.* **51**, 539–572 (2019).

46. G. Fiorucci, J. T. Padding, M. Dijkstra, Small asymmetric Brownian objects self-align in nanofluidic channels. *Soft Matter* **15**, 321–330 (2019).

47. A. Chakrabarty et al., Brownian motion of boomerang colloidal particles. *Phys. Rev. Lett.* **111**, 160603 (2013).

48. M. Bechert et al., Controlling transport dynamics of confined asymmetric fibers. *EPL* **126**, 44001 (2019).

49. M. Gruziel et al., Periodic motion of sedimenting flexible knots. *Phys. Rev. Lett.* **121**, 127801 (2018).

50. J. Cappello et al., Transport of flexible fibers in confined microchannels. *Phys. Rev. Fluids* **4**, 034202 (2019).

51. A. M. Słowicka, E. Wajnryb, M. L. Ekiel-Jeżewska, Lateral migration of flexible fibers in Poiseuille flow between two parallel planar solid walls. *Eur. Phys. J. E* **36**, 31 (2013).

52. B. Bet et al., Calculating the motion of highly confined, arbitrary-shaped particles in Hele–Shaw channels. *Microfluid. Nanofluidics* **22**, 77 (2018).

53. F. P. Bretherton, The motion of rigid particles in a shear flow at low Reynolds number. *J. Fluid Mech.* **14**, 284–304 (1962).

54. H. Bruus, Acoustofluidics 1: Governing equations in microfluidics. *Lab Chip* **11**, 3742–3751 (2011).

55. H. Brenner, The Stokes resistance of an arbitrary particle. *Chem. Eng. Sci.* **18**, 1–25 (1963).

56. J. Happel, H. Brenner, "The motion of a rigid particle of arbitrary shape in an unbounded fluid" in *Low Reynolds Number Hydrodynamics*, R. J. Moreau, ed. (Kluwer Academic Publishers Group, 1983), pp. 174–177.

57. S. Kim, S. J. Karrila, "Resistance and mobility relations" in *Microhydrodynamics: Principles and Selected Applications*, H. Brenner, Ed. (Dover Publications, Inc., 2005), pp. 112–115.

58. W. B. Russel, E. J. Hinch, L. G. Leal, G. Tieffenbruck, Rods falling near a vertical wall. *J. Fluid Mech.* **83**, 273–287 (1977).

59. H. Brenner, The Stokes resistance of an arbitrary particle—II: An extension. *Chem. Eng. Sci.* **19**, 599–629 (1964).

60. B. Bet, S. Samin, R. Georgiev, H. B. Eral, R. van Roij, Steering particles by breaking symmetries. *J. Phys. Condens. Matter* **30**, 224002 (2018).

61. K. Tanaka, H. Takada, Microplastic fragments and microbeads in digestive tracts of planktivorous fish from urban coastal waters. *Sci. Rep.* **6**, 34351 (2016).

62. C. M. Rochman et al., Anthropogenic debris in seafood: Plastic debris and fibers from textiles in fish and bivalves sold for human consumption. *Sci. Rep.* **5**, 14340 (2015).

63. Y. Akiyama, T. Egawa, K. Koyano, H. Moriwaki, Acoustic focusing of microplastics in microchannels: A promising continuous collection approach. *Sensor. Actuator. B Chem.* **304**, 127328 (2020).

64. D. Huber, A. Oskooei, X. C. I. Solvas, A. deMello, G. V. Kaigala, Hydrodynamics in cell studies. *Chem. Rev.* **118**, 2042–2079 (2018).

65. D. Dendukuri et al., Modeling of oxygen-inhibited free radical photopolymerization in a PDMS microfluidic device. *Macromolecules* **41**, 8547–8556 (2008).

66. M. Linkert et al., Metadata matters: Access to image data in the real world. *J. Cell Biol.* **189**, 777–782 (2010).

67. P. R. Amestoy, I. S. Duff, J. Koster, J. Y. L'Excellent, A fully asynchronous multifrontal solver using distributed dynamic scheduling. *SIAM J. Matrix Anal. Appl.* **23**, 15–41 (2001).

68. P. R. Amestoy, A. Guermouche, J. Y. L'Excellent, S. Pralet, Hybrid scheduling for the parallel solution of linear systems. *Parallel Comput.* **32**, 136–156 (2006).

69. E. Holzbecher, H. Si, Accuracy tests for COMSOL - and Delaunay meshes. *Proceedings of the COMSOL Conference* (2008). https://www.comsol.nl/paper/accuracy-tests-for-comsol-and-delaunay-meshes-5436. Accessed 19 August 2020.